

# High resolution population density imaging of random scatterers with the matched filtered scattered field variance

Mark Andrews, Zheng Gong, and Purnima Ratilal

Department of Electrical and Computer Engineering, Northeastern University, 360 Huntington Avenue, Boston, Massachusetts 02115

(Received 11 February 2009; revised 16 June 2009; accepted 17 June 2009)

The matched filter enables imaging with high spatial resolution and high signal-to-noise ratio by coherent correlation with the expected field from what is assumed to be a discrete scatterer. In many physical imaging systems, however, returns from a large number of randomized scatterers, ranging from thousands to millions of individuals, are received together and the coherent or expected field vanishes. Despite this, it is shown that cross-spectral coherence in the matched filtered variance retains a pulse compression property that enables high-resolution imaging of scatterer population density. Analytic expressions for the statistical moments of the broadband matched filtered scattered field are derived in terms of the medium's Green's function, object scatter function, and spatial distribution using a single-scatter approximation. The formulation can account for potential dispersion in the medium and target over the signal bandwidth, and can be used to compare the relative levels of the coherent and incoherent scattered intensities. The analytic model is applied to investigate population density imaging of fish distributions in the Gulf of Maine with an ultrasonic echosounder. The results are verified with numerical Monte-Carlo simulations that include multiple scattering, illustrating that the single-scatter approximation is valid even for relatively dense Atlantic herring (*Clupea harengus*) schools. © 2009 Acoustical Society of America.

[DOI: 10.1121/1.3177271]

PACS number(s): 43.30.Pc [RCG]

Pages: 1057–1068

## I. INTRODUCTION

The matched filter is applied in many remote sensing systems to provide high-resolution imaging of groups of objects or organisms. In underwater sonar applications, scattered returns are matched filtered to determine the population density of fish and other marine organism,<sup>1,2</sup> localize underwater vehicles,<sup>3</sup> and image seafloor and sub-bottom geomorphology.<sup>4</sup> The matched filter has also been used to image migrating bird populations with radar for ecological surveys.<sup>5</sup> Matched filter theory for maximizing signal-to-noise ratio and improving spatial resolution in the detection and localization of a discrete target is well established.<sup>6–8</sup> It is a coherent process implemented by correlating the target generated or scattered field with a replica waveform, which for an active system is usually the transmitted source signal. This pulse compression leads to a range resolution  $\Delta r = c/2B$ , where  $c$  is the wave speed and  $B$  is the signal bandwidth. In contrast, without pulse compression, range resolution  $\Delta r = c\tau/2$  is determined by signal duration  $\tau$  and requires short duration pulses to achieve the same resolution. The matched filter then allows long duration broadband waveforms to be transmitted with sufficient energy to illuminate a target above background noise and still maintain high spatial resolution.<sup>6–8</sup>

When many random scatterers are present, such as an independently moving group of objects, it is typically assumed that the number of scatterers in a given resolution cell is proportional to the intensity of that cell.<sup>1,2,5</sup> This implies a summation of the fields from each scatterer, where upon averaging multiple measurements of the scattered returns from

the randomized group, the expected field or coherent intensity is negligible and the expected intensity is dominated by the variance.<sup>9–12</sup> It is also typically assumed that the resolution cell in range for incoherent returns after matched filtering is defined by the source signal's autocorrelation function.<sup>1,2,5,7,8,13</sup> Analytic solutions for the statistically coherent and incoherent intensities scattered from randomized groups have been formulated in the literature<sup>9–12</sup> but have generally not included the matched filter.

Here the authors show that the incoherently scattered intensity maintains spatial resolution through *cross-spectral coherence* in the matched filtered variance. A full field theory is presented for the statistical moments of the broadband matched filtered field simultaneously scattered from a random distribution of scatterers when the single scattering approximation is valid. The moments depend on the characteristic function of the scatterer's spatial distribution, which may extend over multiple range resolution cells of the imaging system. The moments are the output of a filtering process involving the characteristic function, source spectrum, scatter function, and Green's function. For the mean field, the characteristic function is filtered over a bandwidth centered at the *carrier frequency*. This leads to oscillatory contributions from cross-spectral products in the coherent intensity that are insignificant, on average, over the large spatial extent of the scatterers. On the other hand, the variance of the field depends on the characteristic function filtered at the probing signal's *baseband*, leading to a stable output upon averaging. The variance is shown to resample the scatterer distribution at a spatial rate inversely proportional to the signal bandwidth. Since the scatter function and Green's function are

employed, the model can account for dispersion caused by the target or medium.

The analytic model is applied to the physical example of imaging a school of Atlantic herring in the water column with an ultrasonic echosounder. High-resolution population density imaging of scatterer distributions can be achieved using the matched filtered variance since it is directly proportional to the mean number of scatterers within each resolution cell. The results are verified using numerical Monte-Carlo simulations of the matched filtered scattered field statistics that include multiple scattering. The single-scattering approximation is shown to be valid for imaging Atlantic herring schools exhibiting relatively high volumetric densities near 1 fish/m<sup>3</sup> observed in the Gulf of Maine with an echosounder.

An advantage of the analytic and numerical models developed here is that scattering from the entire distribution extending over multiple range resolution cells of the imaging system, within the sonar beam, can be simultaneously analyzed. By applying the matched filter theory from first principles, scatterers over the entire distribution are automatically localized in range, thereby avoiding the need to artificially break-up the scatterers in the distribution to within each range resolution cell. We provide conditions for when the incoherent scattering assumption is valid for the scatterer distribution and when coherent effects can be neglected. We show that it depends on the distribution size, shape, and scatterer density.

## II. ANALYTIC MODEL FOR STATISTICAL MOMENTS OF MATCHED FILTERED SCATTERED FIELD FROM A GROUP OF RANDOM SCATTERERS

Here we formulate the theory for an active bistatic imaging system, comprised of a source located at  $\mathbf{r}_0$ , and a receiving array located at the origin of the coordinate system, imaging a group of scatterers centered at location  $\mathbf{r}$  in the far-field of both the source and receiver. The formulation assumes that the receiver is not in the forward scatter direction, so that the scattered field at the receiver can be separated from the incident field. The position of any scatterer in the group is  $\mathbf{r}_p = \mathbf{r} + \mathbf{u}_p$ , where  $\mathbf{u}_p$  is its displacement from the group center. The source transmits a broadband waveform  $q(t)$  with Fourier transform  $Q(f)$  and bandwidth  $B$ . For imaging systems used when only single scattering from each object is significant, the time-harmonic scattered field received from the group can be expressed by summing the contribution from each scatterer,<sup>9,10,12,14,15</sup>

$$\Phi_s(\mathbf{r}, f) = Q(f) \sum_p W(\mathbf{r}_p) W_0(\mathbf{r}_p) G(\mathbf{r}_p | \mathbf{r}_0, f) G(\mathbf{0} | \mathbf{r}_p, f) \times \frac{S_p(\Omega_i, \Omega, k)}{k}, \quad (1)$$

where  $W(\mathbf{r}_p)$  and  $W_0(\mathbf{r}_p)$  are the beampatterns of the imaging system source and receiver, respectively, weighting the contribution from the  $p$ th scatterer,  $G$  is the medium's Green's function, and  $S_p(\Omega_i, \Omega, k)$  is the scatter function, which depends on the wavenumber  $k = 2\pi f/c$ , incident angle from the source  $\Omega_i$ , and scattered angle in the direction of the receiver

$\Omega$ . The individual scatterers in the group can be of arbitrary size compared to the wavelength. Here, the group center is assumed to coincide with the main response axis of the receiving array such that the beampattern may be approximated as  $W(\mathbf{r}_p)W_0(\mathbf{r}_p) \approx 1$  for scatterers within the main lobe of the array, and  $W(\mathbf{r}_p)W_0(\mathbf{r}_p) \approx 0$  for scatterers outside of this lobe. Therefore the sum in Eq. (1) is restricted to  $N$ , the total number of scatterers imaged within the main lobe of the imaging system, over the full range extent of the group's distribution. Let  $\mathbf{k}_i$  and  $\mathbf{k}_s$  be the incident and scattered wave vectors for scatterers within the mainlobe in Eq. (1). Approximating the spherical spreading loss, Green's function to each scatterer can be simplified as

$$G(\mathbf{r}_p | \mathbf{r}_0, f) = \frac{e^{ik|\mathbf{r}_p - \mathbf{r}_0|}}{4\pi|\mathbf{r}_p - \mathbf{r}_0|} \approx G(\mathbf{r} | \mathbf{r}_0, f) e^{ik_i \cdot \mathbf{u}_p}, \quad (2)$$

where Green's function from the source to the group center is factored out since the scatterer distribution is in the far-field of both the source and receiver. Using similar approximations for the Green's functions from scatterers to receiver, the scattered field from Eq. (1) now simplifies to

$$\Phi_s(\mathbf{r}, f) = Q(f) G(\mathbf{r} | \mathbf{r}_0, f) G(\mathbf{0} | \mathbf{r}, f) \sum_{p=1}^N e^{j(\mathbf{k}_i - \mathbf{k}_s) \cdot \mathbf{u}_p} \frac{S_p(\Omega_i, \Omega, k)}{k}. \quad (3)$$

The matched filter is now applied,<sup>6-8,16</sup> which is typically a normalized replica of the original transmitted waveform expressed as

$$H(f | t_M) = \frac{1}{\sqrt{E_0}} Q^*(f) e^{i2\pi f t_M}, \quad (4)$$

where  $t_M$  is the time delay of the matched filter and  $E_0 = \int |Q(f)|^2 df$  is the source energy. Using Fourier synthesis, the time-dependent matched filtered scattered signal from Eq. (3) is

$$\Psi_s(t_M) = \int \frac{1}{k} \sum_{p=1}^N e^{i(\mathbf{k}_i - \mathbf{k}_s) \cdot \mathbf{u}_p} S_p(\Omega_i, \Omega, k) \Xi(f) df, \quad (5)$$

where

$$\Xi(f) = \frac{1}{\sqrt{E_0}} |Q(f)|^2 G(\mathbf{r} | \mathbf{r}_0, f) G(\mathbf{0} | \mathbf{r}, f) e^{-i2\pi f(t - t_M)}. \quad (6)$$

The matched filtered signal in Eq. (5) depends on the phase contribution from each scatterer, and is randomized by  $N$ , the total number of scatterers imaged within the sonar beam,  $\mathbf{u}_p$  and  $S_p$ , the location and scatter function for each scatterer, respectively. In general, the position  $\mathbf{u}_p$  can be a function of time.

The expected intensity of the matched filtered scattered returns is a sum of the mean field squared  $|\langle \Psi_s(t_M) \rangle|^2$ , or coherently scattered intensity, and the variance  $\text{var}(\Psi_s(t_M))$ , or incoherently scattered intensity. If we assume the random variables  $N$ ,  $\mathbf{u}_p$ , and  $S_p$  are mutually uncorrelated and the scatterers are identically distributed, then the mean squared matched filtered scattered field becomes

$$\begin{aligned}
|\langle \Psi_s(t_M) \rangle|^2 &= \left| \int \frac{1}{k} \left\langle \sum_{p=1}^N e^{j(\mathbf{k}_i - \mathbf{k}_s) \cdot \mathbf{u}_p} S_p(\Omega_i, \Omega, k) \right\rangle \Xi(f) df \right|^2 \\
&= \langle N \rangle^2 \left| \int \frac{1}{k} U(\mathbf{k}_i - \mathbf{k}_s) S(\Omega_i, \Omega, k) \Xi(f) df \right|^2. \quad (7)
\end{aligned}$$

Here,  $U(\boldsymbol{\kappa})$  is the characteristic function,<sup>14,17</sup>

$$U(\boldsymbol{\kappa}) = \langle e^{j\boldsymbol{\kappa} \cdot \mathbf{u}} \rangle = \int e^{j\boldsymbol{\kappa} \cdot \mathbf{u}} p_{\mathbf{u}}(\mathbf{u}) d\mathbf{u}, \quad (8)$$

which is a three-dimensional spatial Fourier transform of probability density function (PDF)  $p_{\mathbf{u}}(\mathbf{u})$  of scatterer position. The authors assume that the expectation is taken over a measurement time where the distribution is statistically stationary. The coherent intensity in Eq. (7) depends on the expected scatter function,  $\langle S(\Omega_i, \Omega, k) \rangle$ , which in general depends on the incident and scattered angles, and the statistics of the shape, size, material properties, and orientation of the scatterers in the group.

The second moment of the matched filtered scattered field from Eq. (5),

$$\begin{aligned}
|\langle \Psi_s(t_M) \rangle|^2 &= \int \int \frac{1}{kk'} \left\langle \sum_{p=1}^N \sum_{q=1}^N e^{j(\mathbf{k}_i - \mathbf{k}_s) \cdot \mathbf{u}_p} e^{-j(\mathbf{k}'_i - \mathbf{k}'_s) \cdot \mathbf{u}_q} \right. \\
&\quad \left. \times S_p(\Omega_i, \Omega, k) S_q^*(\Omega_i, \Omega, k') \right\rangle \Xi(f) \Xi^*(f') df df', \quad (9)
\end{aligned}$$

depends on the correlation between two different particle's

phase contributions and scatter functions. To evaluate Eq. (9), the joint probability distribution function for the scatterers' positions and scatter functions must in general be specified. Here, it is assumed that the scatter functions are statistically independent from each other and from their relative position among the group. Also, the scatterers' relative positions and phase contributions are assumed to be uncorrelated with the majority of the other scatterers within the imaging system resolution footprint. For many groups in nature, such as fish schools, bird flocks, and insect swarms, each scatterer's position depends only on adjacent and nearby scatterers within some small radius,  $r_c$ , beyond which their positions can be considered independent,<sup>18-20</sup> such that

$$\lim_{|\mathbf{u}_p - \mathbf{u}_q| \gg r_c} p(\mathbf{u}_p, \mathbf{u}_q) = p(\mathbf{u}_p) p(\mathbf{u}_q). \quad (10)$$

The correlation between two particle's positions is typically formulated in terms of the pair distribution function,  $g$ ,<sup>9</sup> defined by

$$p(\mathbf{u}_p, \mathbf{u}_q) = \frac{g(\mathbf{u}_p - \mathbf{u}_q)}{V^2}, \quad (11)$$

where  $V$  is the group volume. For scatterers separated by distances greater than  $r_c$ , their positions can be considered independent, as  $g$  approaches unity. When the imaging system beamwidth is much larger than  $r_c$ , the contribution to the total scattered intensity from correlated scatterers is negligible. Under these conditions, the expectation over the scatter functions and phase contributions simplify

$$\begin{aligned}
&\left\langle \sum_{p=1}^N \sum_{q=1}^N e^{j[(\mathbf{k}_i - \mathbf{k}_s) \cdot \mathbf{u}_p - (\mathbf{k}'_i - \mathbf{k}'_s) \cdot \mathbf{u}_q]} S_p(\Omega_i, \Omega, k) S_q^*(\Omega_i, \Omega, k') \right\rangle \\
&= \int \sum_{p=1}^N \sum_{q=1}^N \left[ \langle e^{j[(\mathbf{k}_i - \mathbf{k}_s) \cdot \mathbf{u}_p - (\mathbf{k}'_i - \mathbf{k}'_s) \cdot \mathbf{u}_q]} \rangle \langle S_p(\Omega_i, \Omega, k) S_q^*(\Omega_i, \Omega, k') \rangle - \langle e^{j(\mathbf{k}_i - \mathbf{k}_s) \cdot \mathbf{u}_p} \rangle \langle e^{-j(\mathbf{k}'_i - \mathbf{k}'_s) \cdot \mathbf{u}_p} \rangle \langle S_p(\Omega_i, \Omega, k) \rangle \langle S_q^*(\Omega_i, \Omega, k') \rangle \right] \delta_{pq} \\
&+ \langle e^{j(\mathbf{k}_i - \mathbf{k}_s) \cdot \mathbf{u}_p} \rangle \langle e^{j(\mathbf{k}'_i - \mathbf{k}'_s) \cdot \mathbf{u}_q} \rangle \langle S_p(\Omega_i, \Omega, k) \rangle \langle S_q^*(\Omega_i, \Omega, k') \rangle \rangle p(N) dN \\
&= \langle N \rangle [U((\mathbf{k}_i - \mathbf{k}_s) - (\mathbf{k}'_i - \mathbf{k}'_s)) \langle S(\Omega_i, \Omega, k) S^*(\Omega_i, \Omega, k') \rangle - U(\mathbf{k}_i - \mathbf{k}_s) U^*(\mathbf{k}'_i - \mathbf{k}'_s) \langle S(\Omega_i, \Omega, k) \rangle \langle S^*(\Omega_i, \Omega, k') \rangle] \\
&+ \langle N^2 \rangle U(\mathbf{k}_i - \mathbf{k}_s) U^*(\mathbf{k}'_i - \mathbf{k}'_s) \langle S(\Omega_i, \Omega, k) \rangle \langle S^*(\Omega_i, \Omega, k') \rangle, \quad (12)
\end{aligned}$$

where  $\delta_{pq}$  is the Kronecker delta and  $p(N)$  is the probability of finding  $N$  scatterers in the group. Inserting Eq. (12) into Eq. (9) results in the following expression for the second moment,

$$\begin{aligned}
|\langle \Psi_s(t_M) \rangle|^2 &= \int \int \frac{1}{kk'} \left( \langle N \rangle [U((\mathbf{k}_i - \mathbf{k}_s) - (\mathbf{k}'_i - \mathbf{k}'_s)) \langle S(\Omega_i, \Omega, k) S^*(\Omega_i, \Omega, k') \rangle - U(\mathbf{k}_i - \mathbf{k}_s) U^*(\mathbf{k}'_i - \mathbf{k}'_s) \langle S(\Omega_i, \Omega, k) \rangle \langle S^*(\Omega_i, \Omega, k') \rangle] \right. \\
&\quad \left. \times \Xi(f) \Xi^*(f') + \langle N^2 \rangle U(\mathbf{k}_i - \mathbf{k}_s) U^*(\mathbf{k}'_i - \mathbf{k}'_s) \langle S(\Omega_i, \Omega, k) \rangle \langle S^*(\Omega_i, \Omega, k') \rangle \right) \Xi(f) \Xi^*(f') df df'. \quad (13)
\end{aligned}$$

The second moment can be expressed as the sum of the coherent intensity in Eq. (7) and the incoherent intensity given by the variance of the field,

$$\begin{aligned}
\text{var}(\Psi_s(t_M)) &= |\langle \Psi_s(t_M) \rangle|^2 - |\langle \Psi_s(t_M) \rangle|^2 = \langle N \rangle \int \int \frac{1}{kk'} [U((\mathbf{k}_i - \mathbf{k}_s) - (\mathbf{k}'_i - \mathbf{k}'_s)) \langle S(\Omega_i, \Omega, k) S^*(\Omega_i, \Omega, k') \rangle \\
&\quad - U(\mathbf{k}_i - \mathbf{k}_s) U^*(\mathbf{k}'_i - \mathbf{k}'_s) \langle S(\Omega_i, \Omega, k) \rangle \langle S^*(\Omega_i, \Omega, k') \rangle] \Xi(f) \Xi^*(f') df df' + \frac{\text{var}(N)}{\langle N \rangle^2} |\langle \Psi_s(t_M) \rangle|^2. \quad (14)
\end{aligned}$$

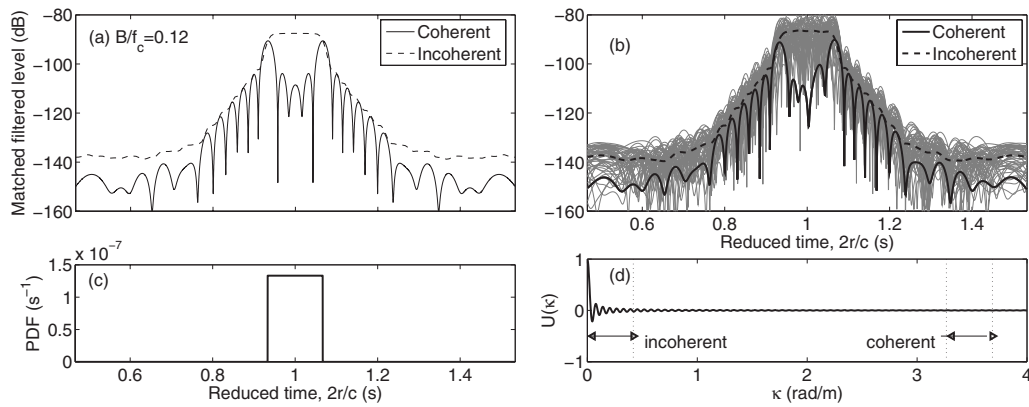


FIG. 1. Broadband matched filtered coherent and incoherent intensity levels scattered from a group of discrete scatterers following a statistically uniform spatial distribution calculated using (a) the analytic model and verified by (b) Monte-Carlo simulations. The spatial PDF for the scatterer distribution is shown in (c) and its wavenumber spectrum in (d). The wavenumber region evaluated by the analytic model coherent intensity corresponding to the source frequency band and the incoherent intensity using the baseband are indicated.

The coherent intensity in Eq. (7) is proportional to  $\langle N \rangle^2$ . If the standard deviation in the number of scatterers is small compared to its mean, then the incoherent intensity in Eq. (14) is proportional to  $\langle N \rangle$ . This is important for population density imaging, since population estimation from the matched filtered intensity depends on whether scattering from a group is coherent or incoherent.

An expression is provided for the incoherent matched filtered intensity in the time domain in Refs. 8 and 13 as the output of a convolution between the magnitude square autocorrelation function of the source signal with the mean backscatter cross-section spatial distribution of the scatterer. This causes complications when there is dispersion in the medium or target since the pulse shape may be altered leading to changes in the range resolution. Furthermore, the incoherent intensity expression in Ref. 8 is only valid when the total number of scatterers in each resolution cell is a constant over time or when the coherent intensity is significantly smaller than the variance, as can be seen by comparison with Eq. (14) in this paper. The matched filtered intensity scattered from a continuum is derived in Eq. (13) of Ref. 21 for the ocean seafloor reverberation. However, the final expression for the expected matched filtered intensity, Eq. (14) of Ref. 21, does not retain the time-frequency exponential dependence. This term is essential, along with the wavenumber dependent term for describing how the variance retains high spatial resolution, as can be seen by comparison with Eq. (14) in this paper.

In practical imaging systems, the matched filtered scattered signal and its intensity as a function of time are charted to range by multiplying with the propagation speed of the signal and accounting for the distance travelled from source to scatterer and from scatterer to receiver.

### III. ILLUSTRATIVE EXAMPLES

In this section, the analytic model is demonstrated with several canonical spatial distributions of scatterer groups. First, the analytic model results for the matched filtered scattered field statistics are verified with numerical Monte-Carlo simulation in Sec. III A. The effect of scatterer distribution size and shape on the relative levels of coherent and incoherent

scattered intensities is examined in Sec. III B. Next, in Sec. III C, the effect of imaging system bandwidth on the spatial resolution of the matched filtered variance is investigated, and it is shown that population density of the scatterers can be inferred from the variance in Sec. III D. Finally, in Sec. IV, the analytic model is applied to the physical example of imaging over depth a school of Atlantic herring, with a relatively large volumetric density of 1 fish/m<sup>3</sup> using an ultrasonic echosounder. The analytic model results are verified with numerical Monte-Carlo simulations that include multiple scattering.

For simplicity, the authors consider only monostatic imaging systems such that  $(\mathbf{k}_i - \mathbf{k}_s) \cdot \mathbf{u}_p \approx 2kx_p$ , so that imaging is achieved with mainly backscattered fields. This simplifies the characteristic function in Eq. (8) to an integration only over range, in this case the  $x$ -direction. In all examples, the scatterer groups are located within the main lobe of the receiver, to investigate only the effects of the matched filtered returns in time.

#### A. Verifying analytic model results with numerical Monte-Carlo simulations for matched filtered field statistics

The analytically determined coherent and incoherent matched filtered scattered intensities are shown in Fig. 1(a) for a group of discrete scatterers centered at  $2r/c=1$  s whose spatial distribution follow the uniform PDF in Fig. 1(c). The intensities are calculated directly from Eqs. (7) and (14). The incoherent intensity dominates the scattered field over the entire range extent of the group except for the edges of the distribution where the coherent intensity is non-negligible. For this example, the temporal extent is  $2L/c=2/15$  s, where  $L$  is the spatial extent of the distribution, and the mean spatial density per unit range for the scatterers is  $\langle N \rangle/L = 100/\text{m}$ . We set  $E_0=1$ , and  $\langle |S/k|^2 \rangle = 1$  which is proportional to the scattering cross-section of an individual scatterer. For this example, the bandwidth is set to  $B/f_c=0.12$ , which is a typical bandwidth-to-carrier frequency ratio for many ocean acoustic imaging systems.<sup>1,2,4</sup> The corresponding matched filter temporal resolution  $2\Delta r/c=1/B=20$  ms.

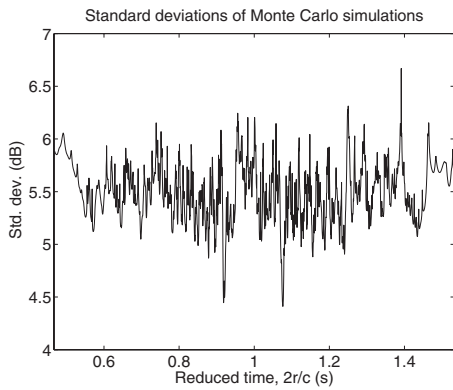


FIG. 2. The standard deviations for the Monte-Carlo simulations for the log transformed matched filtered intensity levels shown in Fig. 1(b).

The results in Fig. 1(a) are verified using Monte-Carlo simulation with 500 realizations in Fig. 1(b), where the locations of the scatterers for each realization are randomly drawn from the uniform spatial PDF of Fig. 1(c). The matched filtered scattered field for each realization is calculated using Eq. (5), and the coherent and incoherent intensities are computed directly as the mean square and variance of the numerical simulations. The analytic model results in Fig. 1(a) are in good agreement with the Monte-Carlo simulation results in Fig. 1(b).

For this distribution, the matched filtered signal behaves as a circular complex Gaussian random process, which implies that the broadband returns are statistically saturated. This can be predicted from Eq. (5) by randomizing the phase from each  $p$ th scatterer according to a uniform PDF. For the uniform PDF used here, the extent of the distribution is significantly larger than the wavelength so that the phase of the scattered returns are essentially also uniformly distributed.

The log transformed intensity realizations illustrated in gray in Fig. 1(b) have a standard deviation near 5.6 dB, as shown in Fig. 2. This indicates that the scattered broadband returns are statistically saturated, such that the intensity measurements are independent realizations of a circular complex Gaussian random field.<sup>17,22,23</sup> The fluctuations in the scattered intensity are entirely a result of the randomness of the scatterers' positions, which randomizes the phase in the scattered returns. This can also be predicted by applying the central limit theorem to Eq. (5), and noting that the phase from each  $p$ th scatterer follows a uniform PDF when the group's distribution is much larger than a wavelength. The example illustrated here is for a deterministic environment,

where the incident intensity does not fluctuate. For an imaging scenario where the environment introduces its own fluctuations, the standard deviations of the scattered returns may differ. In practical imaging systems, the expected matched filtered intensity is measured by averaging over several matched filtered returns to reduce the variance in the estimation of the scatterer population.<sup>17,22,23</sup>

## B. Effect of scatterer distribution size and shape on relative levels of coherent and incoherent matched filtered intensities

Here the analytic intensity results obtained for the scatterer group that follows the uniform spatial distribution in Fig. 1 are compared to another two groups that follow Gaussian spatial distributions for the same imaging system. Figure 3 illustrates the coherent and incoherent scattered intensities for a group of scatterers following a Gaussian spatial PDF with extent (a)  $\sigma_L = 8\lambda$  and (b)  $\sigma_L = \lambda/8$ , respectively, where  $\sigma_L$  is the standard deviation of the group's distribution in range. The scatterer groups in Figs. 1 and 3(a) have the same number of scatterers as well as the same spatial standard deviation for their distributions in range. For the Gaussian distribution in Fig. 3(a), the incoherent intensity dominates over the entire spatial extent of the group unlike the uniform distribution case where the edge effects are non-negligible. Comparing Figs. 3(a) and 3(b), the incoherent intensity dominates until the spatial extent of the distribution is reduced to below a wavelength where the coherent intensity then becomes dominant. The point where the coherent intensity overtakes the incoherent intensity depends largely on the number of scatterers,  $N$ , because the incoherent intensity, given by Eq. (14), is proportional to  $N$ , while the coherent intensity, given by Eq. (7), is proportional to  $N^2$ . For a given spatial distribution, larger numbers of scatterers increase the significance of the coherent intensity.

The characteristic functions  $U(\kappa)$  for the uniform and the two Gaussian spatial distributions are shown in Figs. 1(d) and 3(c), respectively. For the uniform case,  $U(\kappa) = \text{sinc}(\kappa L/2)$ , while the characteristic function for the Gaussian spatial distribution is also Gaussian. The coherent intensity in Eq. (7) filters the characteristic function at the carrier frequency where the larger scatterer groups have significantly smaller amplitudes. Furthermore the cross-spectral products  $U(2k)U^*(2k')$  in the coherent intensity are highly oscillatory leading to cancellation except when the group's spatial extent is small compared to the wavelength or where

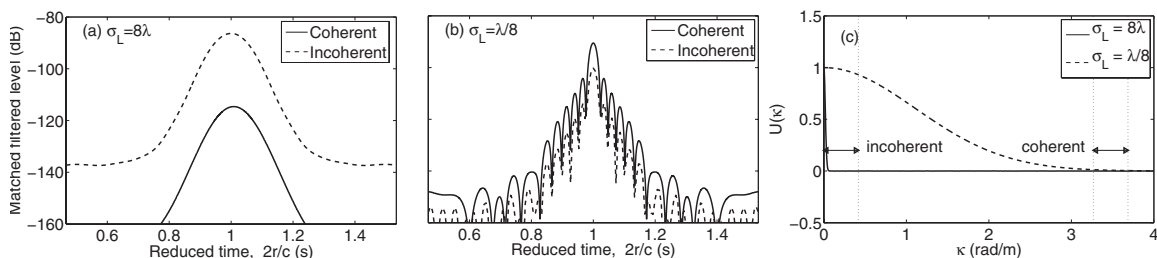


FIG. 3. Broadband matched filtered coherent and incoherent intensity levels scattered from a group of discrete scatterers following a Gaussian spatial PDF with group range extent defined by (a)  $\sigma_L = 8\lambda$  and (b)  $\sigma_L = \lambda/8$ . Their respective characteristic functions are illustrated in (c) where the wavenumber region evaluated by the analytic model coherent intensity corresponding to the source frequency band and the incoherent intensity using the baseband are indicated.

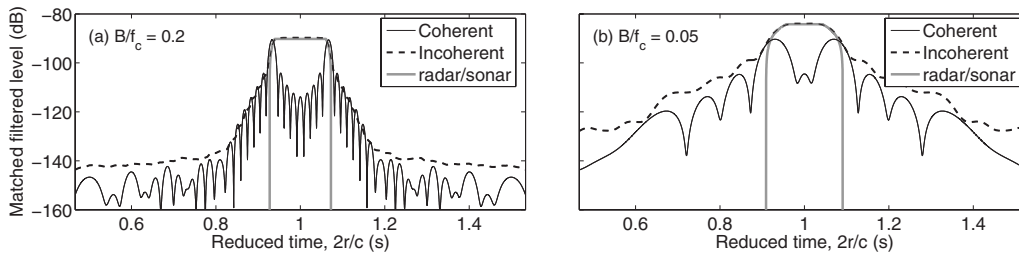


FIG. 4. Effect of varying signal bandwidth to (a)  $B/f_c=0.2$  and (b)  $B/f_c=0.05$ , in comparison with Fig. 1(a). The radar/sonar approximation given by Eq. (15) is plotted over the scattered intensities for the uniform distribution of scatterers with PDF shown in Fig. 1(c).

it has sharply defined edges. In contrast, the incoherent intensity in Eq. (14) filters the characteristic function  $U(2(k-k'))$  at the signal's baseband  $(k-k')=2\pi(f-f')/c$ , where the amplitude is significant for the larger groups. As a result of demodulation to baseband, the variance exhibits cross-spectral coherence that leads to a stable output upon averaging.

### C. Effect of imaging system bandwidth on spatial resolution of matched filtered variance

The effect of the imaging system bandwidth on the matched filtered field statistics is investigated in Fig. 4 for the scatterer group that follows the uniform spatial PDF shown in Fig. 1(c). Comparing Fig. 1(a) with Fig. 4(a), increasing the relative signal bandwidth from  $B/f_c=0.12$  to  $B/f_c=0.2$  provides the matched filtered variance with a larger window in wavenumber to filter the characteristic function. From sampling theory, this allows the scatterer distribution to be sampled with higher spatial resolution  $\Delta r=c/2B$  inversely proportional to the signal bandwidth. The variance reconstructs the spatial distribution, maintaining the higher wavenumber fluctuations. In this example, the reduced time resolution is improved from  $2\Delta r/c=20$  ms to  $2\Delta r/c=12$  ms. Decreasing the system bandwidth, as illustrated in Fig. 4(b), has the effect of sampling the distribution with a low pass filter leading to blurring of the distribution edges. Here, a bandwidth of  $B/f_c=0.05$  leads to a reduced time resolution of  $2\Delta r/c=48$  ms. While this example can be applied for various imaging systems and frequencies, here  $f_c=415$  Hz and  $c=1500$  m/s are used for spatial resolutions of  $\Delta r=9$  m and  $\Delta r=36$  m for (a) and (b) respectively.

These examples illustrate that the variance retains the fine spatial resolution expected of the matched filter, while this analysis here is for a monostatic system, similar analysis can be carried out for bistatic systems in other non-forward scatter directions, applying Eqs. (7) and (14) with the appropriate characteristic function. However, for bistatic systems, the spatial resolution in range depends not only on the temporal resolution of the matched filtered returns but also on the geometry of the problem.

### D. Population density estimation using the incoherent matched filtered intensity

When incoherent scattering dominates, the log-transformed matched filtered variance can be approximated for each resolution cell of the imaging system as

$$L_p(\mathbf{r}_M) \approx L_s + \text{TL}_b(\mathbf{r}_M|\mathbf{r}_0) + \text{TL}_b(\mathbf{0}|\mathbf{r}_M) + \text{TS}_b + 10 \log_{10}(\langle M(\mathbf{r}_M|\Delta r) \rangle), \quad (15)$$

where  $L_p(\mathbf{r}_M)=10 \log_{10} \text{var}(\Psi_s(t_M))$ ,  $L_s=10 \log_{10} E_0$ ,  $\text{TL}_b(\mathbf{r}_M|\mathbf{r}_0)=10 \log_{10} (1/E_0) \int |Q(f)|^2 |G(\mathbf{r}_M|\mathbf{r}_0, f)|^2 df$  is the broadband source spectrum weighted transmission loss,  $\text{TS}_b=10 \log_{10} (1/E_0) \int |Q(f)|^2 (\langle |S(f)|^2 \rangle / k^2) df$  is the broadband source spectrum weighted mean target strength, and  $\langle M(\mathbf{r}_M|\Delta r) \rangle$  is the mean number of scatterers within the resolution footprint at  $\mathbf{r}_M$ . Equation (15) resembles the sonar/radar equation except that it uses the broadband spectrum weighted values. It is in a form that can readily be used to invert for population density imaging, solving for  $M$  across the image. Assuming a flat source spectrum across the bandwidth leads to the familiar sonar equation.

The log-transformed level,  $L_p$  from Eq. (15) is plotted in Fig. 4 using the population density directly. Here, we see the analytic model matches the results well in the region containing the scatterers, as shown in Fig. 4. This implies that the mean intensity obtained by incoherently averaging matched filtered data can be used to infer scatterer population density when the group's spatial distribution is statistically stationary over the averaging time period by correcting for source power, and spectrum weighted transmission losses and target strength.

## IV. IMAGING DENSE SCHOOLS OF FISH WITH AN ULTRASONIC ECHOSOUNDER

The results of Sec. II and the illustrative examples in Sec. III depend on the single-scatter assumption, which is the basis for population density imaging by incoherent summation. The single scattering assumption also implies that attenuation through the group is insignificant. Here, the authors develop a numerical Monte-Carlo simulation model that includes multiple scattering for the statistics of the broadband matched filtered scattered field from a random group of scatterers. The model can be used to determine the conditions for when the single scattering approximation is valid. We compare the results of our analytic model with the single scatter assumption to those of the numerical Monte-Carlo simulation model that includes multiple scattering.

## A. Numerical Monte-Carlo simulation model including multiple scattering for the statistics of the broadband matched filtered scattered field

Given a distribution of scatterers, we first generate the time harmonic singly and multiply scattered fields following the approach of Refs. 9 and 24 but generalized for arbitrarily large scatterers with angular dependent scatter functions. Given a source at  $\mathbf{r}_0$ , receiver at  $\mathbf{r}$  and a group of  $N$  scatterers, where the position of each scatterer is known, the total scattered field at frequency  $f$ ,

$$\Phi_s(\mathbf{r}, f) = \sum_{p=1}^N \Phi_s(\mathbf{r}; p, f), \quad (16)$$

is a sum of the scattered fields from each of the  $p$ th scatterers,

$$\begin{aligned} \Phi_s(\mathbf{r}; p, f) = & Q(f)W(\mathbf{r}_p)G(\mathbf{r}_p|\mathbf{r}_0, f)G(\mathbf{r}|\mathbf{r}_p, f) \frac{S_p(\Omega_i, \Omega, k)}{k} \\ & + \sum_{q=1, q \neq p}^N \Phi_s(\mathbf{r}_p; q, f)G(\mathbf{r}|\mathbf{r}_p, f) \frac{S_p(\Omega_{qp}, \Omega, k)}{k}, \quad (17) \end{aligned}$$

expressed as a sum of the singly and multiply scattered fields. For cases where multiple scattering is negligible, Eqs. (16) and (17) can be combined to give Eq. (1). Here, the second term in Eq. (17) is the multiply scattered field at  $\mathbf{r}$  from the  $p$ th scatterer, first scattered off all other  $N-1$  scatterers, where  $\Phi_s(\mathbf{r}_p; q, f)$  is the scattered field from the  $q$ th scatterer incident on the  $p$ th scatterer.

In order to solve Eq. (17) for all  $N$  scatterers, the scattered field incident on each scatterer from all other  $N-1$  scatterers must be found. This is expressed as

$$\begin{aligned} \Phi_s(\mathbf{r}_n; p, f) = & Q(f)W(\mathbf{r}_p)G(\mathbf{r}_p|\mathbf{r}_0, f)G(\mathbf{r}_n|\mathbf{r}_p, f) \frac{S_p(\Omega_i, \Omega_{pn}, k)}{k} \\ & + \sum_{q=1, q \neq p}^N \Phi_s(\mathbf{r}_p; q, f)G(\mathbf{r}_n|\mathbf{r}_p, f) \frac{S_p(\Omega_{qp}, \Omega_{pn}, k)}{k}, \quad (18) \end{aligned}$$

where  $n$  and  $p$  are dummy variables indicating that the field is incident on  $n$  scattered from  $p$ . For a group of  $N$  scatterers, there are a total of  $N(N-1)$  of these terms representing the field scattered from one particle onto another. Equation (18) has a similar formulation as Eq. (17) in terms of both singly and multiply scattered fields. The scatter functions are in general dependent on both the incident and scattered angles, where  $\Omega_{qp}$  is the incident angle onto  $p$  scattered from  $q$  and  $\Omega_{pn}$  is the scattered angle from  $p$  scattered onto  $n$ . All of the scattering terms represented by Eq. (18) can be grouped into an  $N(N-1)$  column vector  $\underline{\phi}$ , and solved using an  $N(N-1)$  by  $N(N-1)$  matrix equation

$$\underline{\phi} = \underline{\phi}_1 + \mathbf{A}\underline{\phi}, \quad (19)$$

where  $\underline{\phi}_1$  is the  $N(N-1)$  column vector with each element representing the singly scattered field from one scatterer onto another given by the first term in Eq. (18). The matrix  $\mathbf{A}$  is defined such that the product  $\mathbf{A}\underline{\phi}$  is an  $N(N-1)$  column vector with each element representing the multiply scattered

field from one scatterer onto another given by the second term in Eq. (18). The matrix, Eq. (19), can be rearranged and solved by inverting the  $N(N-1)$  by  $N(N-1)$  matrix,

$$\underline{\phi} = (\mathbf{I} - \mathbf{A})^{-1} \underline{\phi}_1. \quad (20)$$

However, for a large number  $N$  of scatterers, this matrix inversion may not be computationally feasible. Alternatively, it may be solved by first including only singly scattered fields, and then adding subsequent orders of scattering until converging on a stable solution using the recursive relation,

$$\underline{\phi}_n = \underline{\phi}_{n-1} + \mathbf{A}\underline{\phi}_{n-1}, \quad (21)$$

where  $\underline{\phi}_n$  includes all orders of scattering up to the  $n$ th order. Together, Eqs. (16)–(19) describe the multiply scattered field off the scatterer group at frequency  $f$  at receiver  $\mathbf{r}$  taking into account the angular dependence in the scatter function.

The time-dependent matched filtered multiply scattered signal from the scatterer group can now be simulated by calculating the time-harmonic scattered field at discrete frequency intervals over the signal bandwidth and applying Fourier synthesis,

$$\Psi_s(t_M) = \int \Phi_s(\mathbf{r}, f)H(f|t_M)e^{-i2\pi ft}df, \quad (22)$$

where the matched filter  $H(f|t_M)$  is defined in Eq. (4), and the time-harmonic scattered field is found using Eqs. (16)–(18). The statistics of the multiply scattered matched filtered returns from a group of scatterers following a stationary distribution are estimated using a sample of independent Monte-Carlo simulations. For each simulation, the positions and scatter functions of each scatterer are randomly drawn following their specified statistical distributions. The matched filtered signal scattered from the group is then calculated, and the coherent and incoherent intensities are estimated by the sample mean square and sample variance, respectively, over all of the realizations.

An advantage of applying the matched filter to model the multiply scattered fields from a distribution of scatterers using a broadband pulsed signal is that, under certain scenarios, the various orders of scattering can be distinguished through time delays in subsequent orders of scattering. A simple example of multiple scattering is demonstrated in Fig. 5, where the matched filtered returns from two discrete non-random scatterers are simulated using Eq. (22), by integrating over frequency the time harmonic scattered field at the receiver, given by Eqs. (16)–(18). The two scatterers illustrated in Fig. 5(a) are placed equidistant from a monostatic imaging system separated by  $d$  from each other at  $(0, d/2)$  and  $(0, -d/2)$ . For illustrative purposes, the scatterers are given very high target strengths so that the multiple scattering effects stand out for only two scatterers. The imaging system transmits a broadband pulse and the scattered returns at the receiver are matched filtered and charted over range using the two-way travel time,  $r=ct/2$ . Figure 5(b) illustrates the matched filtered scattered returns for three cases: (1) single scattering only, (2) double and single scattering applying the iterative approach, and (3) all orders of scattering using the exact matrix solution. The single scattering pro-

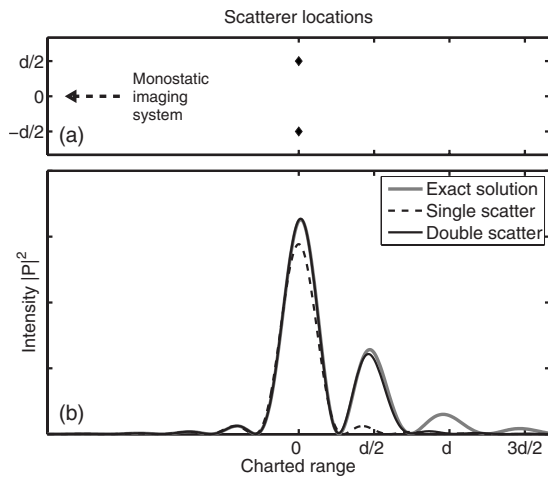


FIG. 5. Broadband matched filtered returns from two non-random discrete targets located at  $(0, -d/2)$  and  $(0, d/2)$  as shown in (a). The effects of multiple scattering can be seen in (b) by comparing the singly scattered to the multiply scattered matched filtered returns. This example was implemented with  $d=60$  m,  $TS=30$  dB, and an imaging system with resolution  $\Delta r=15$  m.

duces a single peak, since the returns from each of the two scatterers are received together. Small sidelobes from the matched filtering process can be seen both before and after the primary peak but are less than 10% of the primary peak. The doubly scattered return exhibits a secondary delayed return due to the longer path length traversed by the second order multiply scattered waves. The main peak is also higher including multiple scattering because the sidelobe of the secondary peak coincides with the primary peak. Similarly, including higher orders of scattering produces noticeably delayed returns. The target strengths need not be as high as illustrated in this example to observe significant multiple scattering effects if the population density is increased. In general, as illustrated in this example, multiple scattering effects are characterized by a higher overall scattering level as well as additional delayed returns.

## B. Application to ultrasonic echosounder imaging of a school of Atlantic herring in the Gulf of Maine

Here we examine population density imaging of a school of Atlantic herring as a function of water depth in the Gulf of Maine with a conventional fish-finding ultrasonic echosounder. The imaging system uses a broadband linear frequency modulated (LFM) waveform processed with a matched filter.

Many fish-finding echosounders use cw pulses for echolocation, where the pulse duration,  $T$ , determines the resolution in depth  $\Delta r=cT/2$ . The resulting signal bandwidth is inversely related to the time duration,  $B=1/T$ . Shorter duration pulses offer better depth resolution, however, suffer from reduced signal to noise ratio.<sup>25</sup> Alternatively, some echosounders transmit longer duration broadband LFM waveforms with sufficient energy to provide high signal-to-noise ratio, while still achieving high resolution by applying a matched filter to the scattered returns. In some cases, this method has been found to sufficiently resolve individual fish. For broadband systems, several issues must be addressed in

order to accurately calibrate as well as image population density. Both source level and beamwidth may vary over the signal bandwidth, changing the amplitude and ensonified volume as a function of frequency. For this reason, short duration cw systems have been more widely used in the fisheries community and have been extensively calibrated. Both types of echosounders systems offer distinct advantages.

Here, a group of herring are imaged with an EK60 Simrad echosounder, operating with a 38 kHz cw pulse, with a duration of 1 ms, a repetition rate of  $1\text{ s}^{-1}$ , and bandwidth  $B=1$  kHz, leading to a spatial resolution in depth of  $\Delta r=0.75$  m for sound speed  $c=1500$  m/s. The imaged fish group is used as a basis for our numerical model in order to simulate observed fish density profiles with a broadband system with a LFM chirp signal with bandwidth  $B=3.75$  kHz. The actual fish density distributions may have fluctuations in depth that were not resolved by the cw system that could be observed by a broadband imaging system. However, the volumetric densities observed here are too high to resolve individual fish, even for most broadband systems. The analysis in this section simulates the echosounder imaging a relatively dense group of herring to show that (1) the incoherent intensity is dominant upon averaging, and (2) multiple scattering is negligible.

Shoaling Atlantic herring populations in the Gulf of Maine typically have volumetric densities near  $0.05\text{ fish/m}^3$ .<sup>26,27</sup> On rare occasions, however, they have been known to cluster in relatively dense schools with volumetric densities of  $1\text{ fish/m}^3$  as was the case for the school observed here. Figure 6(a) shows an echosounder imagery of the herring school centered at 125 m depth in waters 200 m deep acquired at Georges Basin in the Gulf of Maine on September 22, 2006 using a Simrad EK60 echosounder operating at 38 kHz. The school is assumed to be Atlantic herring based on trawl surveys<sup>26</sup> conducted 4 days later, in the same area of the Gulf of Maine, just north of Georges Bank. The trawl surveys identified several fish schools consisting of more than 99% herring. Historical data<sup>28</sup> have also found Atlantic herring to be by far the most abundant schooling fish in the region.

The EK60 echosounder is hull-mounted and directed downward to provide depth profiles of the fish distributions. The echosounder transducer has a conical beamwidth of  $7^\circ$ , horizontal circular areal resolution of 183 m with diameter of 15.3 m at 125 m water depth. The data shown in Fig. 6(a) are in terms of volumetric backscatter strength ( $S_v$ ) over depth, with profiles collected over time as the vessel traveled over the fish school at a nominal velocity of 3 m/s.

Volumetric backscatter strength,  $S_v$ , can be converted to population density, illustrated in Fig. 6(b) using an estimated mean target strength of  $-39.6$  dB for individual herring.<sup>29</sup> The volumetric densities shown in Fig. 6(b) are for the region between the vertical solid lines in Fig. 6(a), where the density distributions are approximately stationary in time and space. In practice, the depth-dependent volumetric density profiles are incoherently averaged over range to reduce variance in the estimation of scatterer population.<sup>17,22</sup> The total estimated number of fish,  $N$ , integrated over the depth of the beam has a mean  $\langle N \rangle=1950$  and standard deviation  $\sigma_N$

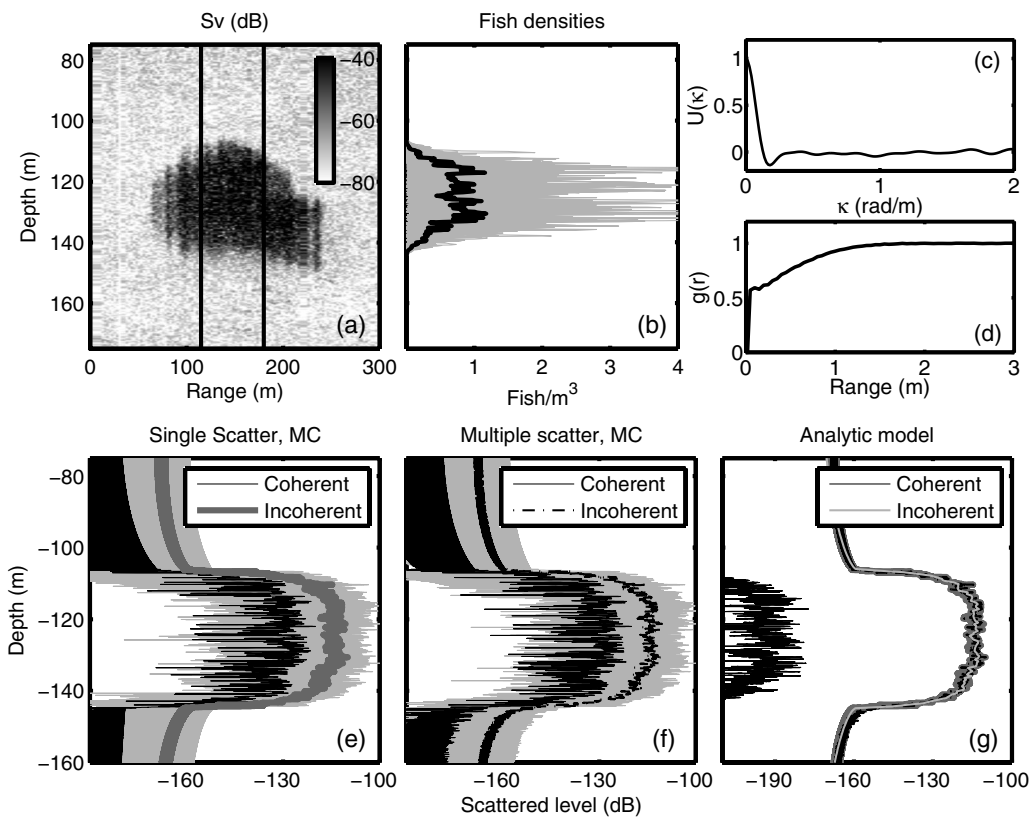


FIG. 6. Broadband matched filtered coherent and incoherent intensity levels scattered from a group of fish. (a) Echosounder data in terms of volumetric scattering strength ( $S_v$ ) are plotted as a function of depth and range. (b) This is converted to volumetric densities in gray using an estimated mean target strength of  $-39.6$  dB for Atlantic herring assuming single-scattering; the mean over the 25 measurements is shown in black. Numerical Monte-Carlo models simulate the matched filtered returns from this group characterized by the pair distribution function,  $g(r)$  illustrated in (d). The Monte-Carlo simulation results using (e) the single-scatter approximation and (f) including multiple scattering show the individual matched filtered signals in light gray, along with the sample mean square, or coherent intensity, and sample variance, or incoherent intensity. Panel (g) compares the incoherent intensities from the numerical Monte-Carlo simulations in (e) and (f) to the coherent and incoherent intensities found using the analytic model. The characteristic function,  $U(k)$ , for this distribution used in the analytic model is illustrated in (c).

$=580$  taken over the 25 depth profile samples measured in the region of interest. The standard deviation,  $\sigma_N$ , is a result of both a variation in the number of fish over range and variations in the herring backscatter target strength and other sources of noise and variation. Regardless of the source of the variation, averaging the volumetric profiles over a statistically stationary region reduces the error in both the mean number of fish,  $\langle N \rangle$ , and the mean volumetric density profile shown in Fig. 6(b). This inversion to volumetric fish density assumes that (1) single scattering is dominant, and (2) the incoherent intensity is dominant over the coherent. Here, the authors show using numerical Monte-Carlo simulations that these assumptions hold even for these relatively dense schools. The analytic model described in Sec. II can then be applied to rapidly compare the matched filtered coherent and incoherent intensities for a variety of fish distributions.

For the numerical Monte-Carlo simulation model, the three-dimensional fish spatial distributions are first generated within the echosounder beam using the fish density profile in Fig. 6(b) to determine their depth dependence and the pair distribution function shown in Fig. 6(d) to determine the inter-fish spacings. Noise in the data and variations in the fish target strength may have resulted in errors in the estimated density profiles. In the Monte-Carlo model, these values are assumed to be correct. By averaging the results of the

Monte-Carlo simulations, they reduce this error, as long as the estimated mean target strength is accurate. The pair distribution function of the herring depends on their individual behaviors and group interactions, and has not been thoroughly quantified although it is an area of ongoing research.<sup>18</sup> For dense groups where several fish occupy a resolution cell, it cannot be determined from the data. Here, the fish are assumed to be distributed according to a uniform PDF within an individual resolution cell, except that they cannot be within the near-field of each other. It can be seen in Fig. 6(d) that the pair distribution function converges to unity near 1 m, which is the approximate mean inter-fish spacing for a density of 1 fish/m<sup>3</sup>.

The primary scattering mechanism for herring imaged at 38 kHz are their air-filled swimbladder.<sup>29-31</sup> It has been found that the Rayleigh-Born scattering from the body of the fish is important at much higher frequencies; however, it has secondary importance at 38 kHz.<sup>30</sup> The herring swimbladder is a complicated three-dimensional air-filled structure.<sup>32</sup> It is usually modeled as a prolate spheroid.<sup>33</sup> Here, for simplicity, the swimbladder is modeled as a pressure-release sphere in the interest of determining whether or not multiple scattering is significant at all. The swimbladder radius is adjusted to

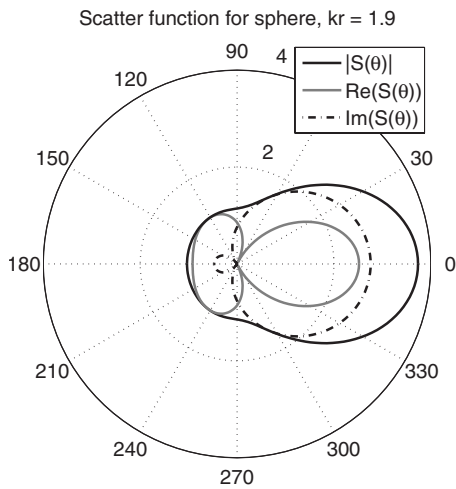


FIG. 7. The angular dependent scatter function for the pressure release sphere used in the numerical and analytic models is illustrated. The magnitude, and real and imaginary parts are plotted in polar coordinates, where  $0^\circ$  indicates the forward scatter direction and  $180^\circ$  indicates backscatter.

have a mean radius  $a=1.2$  cm with standard deviation of 0.2 cm so that the backscattered target strength is consistent with experimentally determined values.<sup>29</sup>

For the herring modeled here, the far-field<sup>15</sup> condition is  $r > 4a^2/\lambda = 1.5$  cm for a 38 kHz echosounder. The scatterers are in the far-field of each other since the mean inter-fish spacing of 1 m is much larger than this distance. Furthermore, the pair distribution function,  $g(r)$ , shown in Fig. 6(d) is defined so that the fish swimbladders are spaced at least 5 cm apart. This is a realistic requirement because the herring body is on average 25 cm in length and roughly 5 cm in width; mean spacing of the herring is larger than this for mean volumetric density of 1 fish/m<sup>3</sup> as well as in the locally very dense regions where the density can be up to 4 fish/m<sup>3</sup>. Since the fish are in each other's far-field, there is negligible attenuation caused by the near-field shadow, which has a length of  $(ka/2)^{1/3}a = 1.2$  cm. At the operating frequency of 38 kHz, the product  $ka \approx 2$  so that the scatterers are non-compact and the angular and range dependent scattered field from the swimbladder can be modeled exactly using Eq. (10.15) of Ref. 34, which includes near-field effects. Since the scatterers here are in the far-field of each other, the scattered field can be approximated by applying the scatter function in Eq. (10.18) of Ref. 34 with negligible error. The half power beam-width of the scatter function employed for the swimbladder at 38 kHz is roughly  $90^\circ$  as shown in Fig. 7.

The broadband matched filtered scattered field simulated using the numerical Monte-Carlo simulation model for 25 realizations of fish distribution within the sonar beam as a function of depth is plotted in gray in Figs. 6(e) and 6(f) for the singly and multiply scattered fields, respectively. In each figure, the sample mean square and variance over the multiple realizations give us the coherent and incoherent intensities. Here the authors see that the incoherent intensity dominates by at least 10 dB. The sample mean square or coherent intensity would be lower had more independent measurements available. Comparing the singly and multiply scattered incoherent matched filtered intensities in Figs. 6(g)

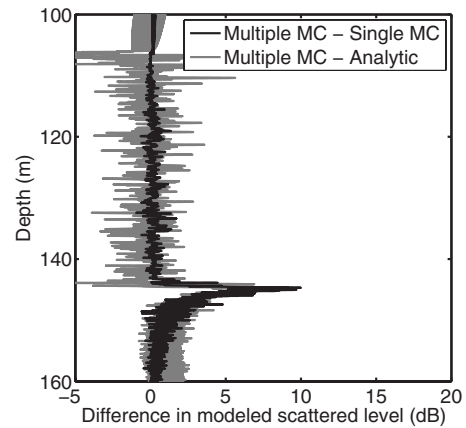


FIG. 8. The differences in the modeled scattered levels from Fig. 6(g) illustrate the effect of multiple scattering over the imaged depth. The difference between the Monte-Carlo multiple scattering model and Monte-Carlo single scattering model is shown in black, while the difference between the Monte-Carlo multiple scattering model and analytic model is shown in gray.

and 8 generated using the Monte-Carlo model, they are found to be nearly identical, except at the tail end of the distribution near 145 m depth where the multiply scattered field is slightly higher due to delayed returns. This difference is negligible for population estimation since it is more than 40 dB down from the densely populated region. The single scattering assumption also implies that the incident acoustic intensity is not significantly attenuated through the fish school.

Since the single-scattering assumption is sufficient for fish schools of the given target strength and density, the analytic model can be used to compare the coherent and incoherent intensities using Eqs. (7) and (14), respectively, shown in Fig. 6(g). The mean distribution in Fig. 6(b) is used as the PDF for Eq. (8). The means and variances of the scatter function  $S(\Omega_i, \Omega, k)$  and the number of scatterers  $N$  used in the analytic model are the same as those used in the Monte-Carlo simulations. Here, we see that the analytic incoherent intensity is in good agreement with the Monte-Carlo result to within 1 dB in the fish region, as shown in Figs. 6(g) and 8. This shows that the correlation between adjacent scatterers has negligible effect on the total intensity and the pair distribution function can be approximated as unity in deriving Eq. (14).

The analytically determined coherent intensity is found to be nearly 80 dB below the incoherent which was not predicted with the numerical models because many more independent realizations would be required to sufficiently converge the sample mean square value to the expected mean square. The convergence of the sample mean square is slow in this case when plotted in log because it is converging to near zero intensity values. Here a drop of more than 10 dB corresponds to a 90% reduction in intensity. Figure 9 illustrates the sample mean square using 4, 12, and all 25 samples to illustrate the slow trend of convergence.

In this section, we could only include up to third order scattering in the Monte-Carlo model because of computational memory constraints. The result obtained here that multiple scattering is negligible for ultrasonic frequency echosounder imaging of dense fish schools is consistent with the

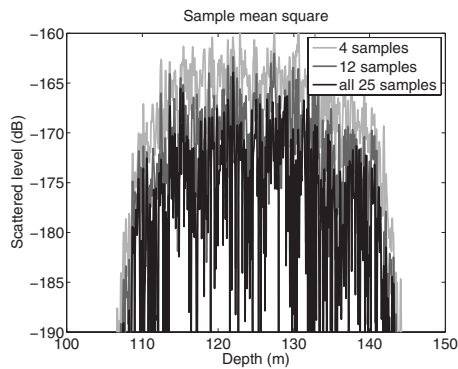


FIG. 9. The coherent intensity for the Monte-Carlo model decreases as more independent samples are added. To obtain the analytic result shown in Fig. 6(g), many more samples would be required.

experimental findings of Ref. 20 and theoretical result of Ref. 35 which considers multiple scattering only up to second order. Both these references, however, do not account for the effects of the matched filter. Further analysis with the three-dimensional Monte-Carlo model developed here indicate that either the fish target strength or volumetric densities need to be 10 dB larger for multiple scattering to matter. These higher densities and target strengths, however, are not realistic for fish distributions that occur in nature.

## V. CONCLUSION

Analytic expressions have been derived from first principles, for the statistical moments of the broadband matched filtered scattered field from a random spatial distribution of random targets. The model is applicable when there is dispersion in the medium or target. The theory and analysis presented here explain how high-resolution population density images of randomly distributed objects or organisms can be obtained through cross-spectral coherence in the matched filter variance. The analytic model can be applied to object distributions where (1) the single-scattering approximation is valid, (2) the scatterers are in the far-field of each other, and (3) the correlation between scatterers makes negligible contribution to the total scattered intensity.

The analytic model is verified with a numerical Monte-Carlo model simulating a distribution of Atlantic herring imaged with an ultrasonic echosounder. The Monte-Carlo model illustrates that multiple scattering is negligible, even for relatively high volumetric densities of 1 fish/m<sup>3</sup>. Upon averaging, the sample variance of the Monte-Carlo model converges to levels predicted by the analytic model. The authors show that the incoherently scattered intensity can be used to image population densities with resolution inversely related to bandwidth,  $\Delta r = c/2B$ .

## ACKNOWLEDGMENTS

This research was funded by the Office of Naval Research, the National Oceanographic Partnership Program and the Alfred P. Sloan Foundation with administrative support from Bernard M. Gordon Center for Subsurface Sensing and Imaging Systems. This research is a contribution to the Census of Marine Life.

- <sup>1</sup>N. C. Makris, P. Ratilal, D. T. Symonds, S. Jagannathan, S. Lee, and R. W. Nero, "Fish population and behavior revealed by instantaneous continental shelf-scale imaging," *Science* **311**, 660–663 (2006).
- <sup>2</sup>D. N. MacLennan and E. J. Simmonds, *Fisheries Acoustics*, 2nd ed. (Chapman and Hall, London, 1992).
- <sup>3</sup>W. S. Burdic, *Underwater Acoustic Systems Analysis* (Prentice-Hall, Englewood Cliffs, NJ, 1984).
- <sup>4</sup>S. Schock, "A method for estimating the physical and acoustic properties of the seabed using chirp sonar data," *Inf. Sci. (N.Y.)* **29**, 1200–1217 (2004).
- <sup>5</sup>E. Eastwood, *Radar Ornithology* (Methuen, London, 1967).
- <sup>6</sup>G. L. Turin, "An introduction to matched filters," *IRE Trans. Inf. Theory* **6**, 311–329 (1960).
- <sup>7</sup>C. E. Cook and M. Bernfeld, *Radar Signals: An Introduction to Theory and Application* (Artech House, Boston, 1993).
- <sup>8</sup>A. W. Rihaczek, *Principles of High-Resolution Radar* (Artech House, Boston, 1996).
- <sup>9</sup>L. Tsang, J. A. Kong, and K.-H. Ding, *Scattering of Electromagnetic Waves: Theories and Applications* (Wiley, New York, 2000).
- <sup>10</sup>J. W. Strohbehn, *Laser Beam Propagation in the Atmosphere* (Springer, Germany, 1978).
- <sup>11</sup>H. C. van de Hulst, *Light Scattering by Small Particles* (Dover, New York, 1957).
- <sup>12</sup>A. Ishimaru, *Wave Propagation and Scattering in Random Media* (Academic, New York, 1978).
- <sup>13</sup>E. N. Fowle, E. J. Kelly, and J. A. Sheehan, "Radar system performance in a dense-target environment," *IRE Int. Conv. Rec.* **4**, 136–145 (1961).
- <sup>14</sup>P. Ratilal and N. C. Makris, "Mean and covariance of the forward field propagated through a stratified ocean waveguide with three-dimensional random inhomogeneities," *J. Acoust. Soc. Am.* **118**, 3532–3559 (2005).
- <sup>15</sup>M. Born and E. Wolf, *Principles of Optics* (Cambridge University Press, Cambridge, 1980).
- <sup>16</sup>N. Levanon, *Radar Principles* (Wiley, New York, 1988).
- <sup>17</sup>J. W. Goodman, *Statistical Optics* (Wiley, New York, 1985).
- <sup>18</sup>J. H. Tien, S. A. Levin, and D. I. Rubenstein, "Dynamics of fish shoals: Identifying key decision rules," *Evol. Ecol. Res.* **6**, 555–565 (2004).
- <sup>19</sup>I. D. Couzin, J. Krause, R. James, G. D. Ruxton, and N. R. Franks, "Collective memory and spatial sorting in animal groups," *J. Theor. Biol.* **218**, 1–11 (2002).
- <sup>20</sup>K. G. Foote, "Linearity of fisheries acoustics, with addition theorems," *J. Acoust. Soc. Am.* **73**, 1932–1940 (1983).
- <sup>21</sup>B. Newhall, "Continuous reverberation response and comb spectra waveform design," *Inf. Sci. (N.Y.)* **32**, 524–532 (2007).
- <sup>22</sup>N. C. Makris, "The effect of saturated transmission of scintillation on ocean acoustic intensity measurements," *J. Acoust. Soc. Am.* **100**, 769–783 (1996).
- <sup>23</sup>B. R. Frieden, *Probability, Statistical Optics and Data Testing*, 3rd ed. (Springer, Germany, 2001).
- <sup>24</sup>Z. Ye and A. Alvarez, "Acoustic localization in bubbly liquid media," *Phys. Rev. Lett.* **80**, 3503–3506 (1998).
- <sup>25</sup>J. E. Ehrenberg and T. C. Torkelson, "Fm slide (chirp) signals: A technique for significantly improving the signal-to-noise performance in hydroacoustic assessment systems," *Fish. Res.* **47**, 193–199 (2000).
- <sup>26</sup>Z. Gong, M. Andrews, D. Tran, D. Cocuzzo, S. Dasgupta, S. Jagannathan, I. Bertsatos, D. Symonds, T. Chen, H. Pena, R. Patel, O. R. Godo, R. W. Nero, J. M. Jech, N. Makris, and P. Ratilal, "Atlantic herring (*clupea harengus*) low frequency target strength and abundance estimation: Ocean acoustic waveguide remote sensing (oawrs) 2006 gulf of maine experiment," *J. Acoust. Soc. Am.* submitted.
- <sup>27</sup>N. C. Makris, P. Ratilal, S. Jagannathan, Z. Gong, M. Andrews, I. Bertsatos, O. R. Godo, R. W. Nero, and J. M. Jech, "Critical population density triggers rapid formation of vast oceanic fish shoals," *Science* **323**, 1734–1737 (2009).
- <sup>28</sup>W. J. Overholtz, J. M. Jech, W. Michaels, L. Jacobson, and P. Sullivan, "Empirical comparisons of survey designs in acoustic surveys of gulf of maine-georges bank atlantic herring," *J. Northw. Atl. Fish. Sci.* **36**, 127–144 (2006).
- <sup>29</sup>E. Ona, "An expanded target strength relationship for herring," *ICES J. Mar. Sci.* **70**, 107–127 (2003).
- <sup>30</sup>K. G. Foote, "Importance of the swimbladder in acoustic scattering by fish: A comparison on gadoid and mackerel target strengths," *J. Acoust. Soc. Am.* **67**, 2084–2089 (1980).

- <sup>31</sup>C. Feuillade, R. W. Nero, and R. H. Love, "A low-frequency acoustic scattering model for small schools of fish," *J. Acoust. Soc. Am.* **99**, 196–208 (1996).
- <sup>32</sup>N. Gorska and E. Ona, "Modelling the effect of swimbladder compression on the acoustic backscattering from herring at normal or near-normal dorsal incidences," *ICES J. Mar. Sci.* **60**, 1381–1391 (2003).
- <sup>33</sup>R. W. Nero, C. H. Thompson, and J. M. Jech, "In situ acoustic estimates of the swimbladder volume of atlantic herring (*clupea harengus*)," *ICES J. Mar. Sci.* **61**, 323–337 (2004).
- <sup>34</sup>J. Bowman, T. Senior, and P. Uslenghi, *Electromagnetic and Acoustic Scattering by Simple Shapes* (North-Holland, Amsterdam, 1969).
- <sup>35</sup>T. Stanton, "Multiple-scattering with applications to fish echo-processing," *J. Acoust. Soc. Am.* **73**, 1164–1169 (1983).